

# A scalable method for the synthesis of high quality topological insulator nanostructures

L. D. Alegria,<sup>1</sup> M. D. Schroer,<sup>1</sup> G. R. Poirier,<sup>1</sup> M. Pretko,<sup>1</sup> A. Chatterjee,<sup>1</sup> S. K. Patel,<sup>1</sup> and J. R. Petta<sup>1</sup>

<sup>1</sup>*Department of Physics, Princeton University, Princeton, NJ 08544, USA.*

(Dated: August 26, 2011)

PACS numbers: 61.46.Km, 73.25.+i, 73.20.At, 78.30.Hv, 73.43.-f, 85.75.-d

**Bi<sub>2</sub>Se<sub>3</sub> is a strong topological insulator (TI) with a single Dirac cone and chiral spin texture [1, 2]. Surface-sensitive probes have directly accessed the topological surface states, but transport measurements have proven difficult due to bulk contributions to the conductivity [3, 4]. Efforts aimed at isolating surface transport properties have focused on mechanical exfoliation, electrical gating, and chemical doping [5–9]. An alternative way to minimize bulk contributions to the conductivity is to synthesize nanostructures with a large surface-to-volume ratio [10, 11]. We demonstrate the controlled synthesis of Bi<sub>2</sub>Se<sub>3</sub> nanostructures with large surface-to-volume ratio using metal-organic chemical vapor deposition (MOCVD), a standard process for large scale production of semiconductor compounds. Simple adjustment of the reactor parameters allows us to obtain highly ordered nanoribbons up to 10  $\mu\text{m}$  long or thin micron sized platelets. The method can be readily extended to produce doped or ternary compounds, enabling future TI transport measurements, efforts to isolate Majorana Fermions, and the development of new thermoelectric materials [12–16].**

Bi<sub>2</sub>Se<sub>3</sub> has been the focus of many TI experiments due to its comparatively large bulk band gap of 0.35 eV and simple surface band structure [3]. The Bi<sub>2</sub>Se<sub>3</sub> crystal is rhombohedral and belongs to the space group  $D_{3d}^5 (R\bar{3}m)$  [17]. The crystal consists of repeated quintuple layers (QLs), each containing Se-Bi-Se-Bi-Se, as illustrated in Fig. 1. Adjacent layers of Se are Van der Waals bonded, such that Bi<sub>2</sub>Se<sub>3</sub> preferentially forms sheet-like structures. As a result, crystals can be mechanically exfoliated down to a single quintuple layer [6, 18]. The weak bonding of Se in the lattice also results in Se vacancies, causing n-type bulk conduction, which has hindered transport measurements [5]. In addition to TI research, Bi<sub>2</sub>Se<sub>3</sub> and related compounds are of interest for high performance thermoelectric materials [16]. Various systems, including quintuple layer nanotubes, have been synthesized by co-reduction from solution, template-assisted electrodeposition, and solid-source vapor transport [19–21]. The latter method has proven useful for several TI experiments [10]. Ultimately, factors including sample purity, uniformity of growth, and tunability of the Se/Bi flux

ratio favor the two workhorses of semiconductor growth, molecular beam epitaxy (MBE) and MOCVD.

We synthesize Bi<sub>2</sub>Se<sub>3</sub> nanostructures in a laboratory-scale MOCVD system based on traditional MOCVD reactor technology [22–24]. A similar growth system has yielded high purity InAs nanowires, which can be locally gated to create single electron quantum dots [25, 26]. Mass flow controllers admit fixed flows of H<sub>2</sub> carrier gas through two bubblers containing the liquid metal-organic precursors trimethyl bismuth (TMBi) and diethyl selenium (DESe) [27]. The precursor vapors and H<sub>2</sub> carrier gas flow into a cold-wall vacuum chamber and impinge on a heated sample holder. The precursors thermally decompose on a Si (100) substrate that is prepared with a 5 nm thick Au seed layer, resulting in Bi<sub>2</sub>Se<sub>3</sub> nanostructure growth, as depicted in Fig. 1. We expect the MOCVD process developed here to be a versatile platform for TI growth, since it allows the growth of doped or ternary compounds that would be difficult to achieve with solid source vapor phase epitaxy [12].

Bi<sub>2</sub>Se<sub>3</sub> nanostructures form for a wide range of growth conditions. We generally obtain two different types of structures: 1) nanoribbons with 10 – 30 nm thickness and lengths of several microns, or 2) nanoplates as thin as 10 nm with roughly 1  $\mu\text{m}$  lateral dimensions. The growth temperature,  $T_g$ , and precursor partial pressure ratio,  $r = P_{\text{DESe}}/P_{\text{TMBi}}$ , determine which type of structures we obtain. Figure 2 shows scanning electron microscope (SEM) images of samples obtained for a range of growth parameters. High-yield growth occurs for  $T_g = 470^\circ\text{C}$ , with a chamber pressure  $P = 100$  Torr, carrier gas flow of 600 sccm H<sub>2</sub>, and  $r = 30$ . Typical growth times are 15 minutes. Under the latter conditions, nanoribbon growth begins once the precursor partial pressure ratio exceeds  $\sim 7$ . Between  $r = 7 - 33$ , the reaction products transition from narrow ribbons to wide ribbons and plates, accompanied by an increase in density. Above  $r = 33$  the morphology appeared constant. We demonstrate the transition in structural properties in Fig. 3 (a), where we plot the density of nanoribbons as a function of precursor ratio. From the data we draw two conclusions: 1) Se limits the growth at low precursor ratios, and 2) the precursor ratio controls the growth anisotropy.

We also study the temperature dependence of the growth. At a fixed precursor ratio  $r = 30$ , nanoribbons are obtained at a growth temperature  $T_g = 470^\circ\text{C}$  and

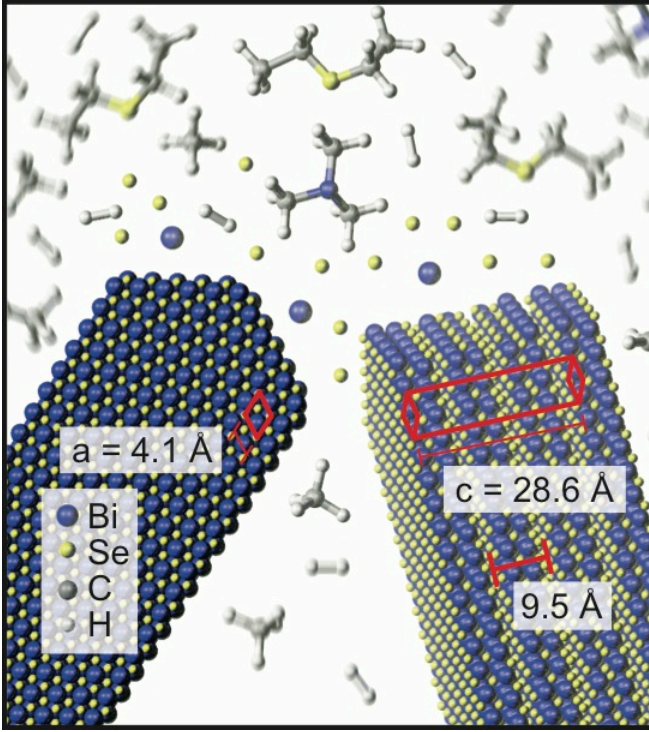


FIG. 1: Schematic of a  $\text{Bi}_2\text{Se}_3$  nanoribbon growing by MOCVD, viewed along the  $c$ -axis (left) and nearly along the  $a$ - $b$  plane (right). Hydrogen carrier gas delivers a dilute vapor of trimethyl bismuth and diethyl selenium precursors to the heated substrate, where they decompose to form elemental Bi and Se, as well as volatile organic products. Bi and Se preferentially attach at dangling bonds on the edge of the  $\text{Bi}_2\text{Se}_3$  crystal.  $\text{Bi}_2\text{Se}_3$  belongs to the  $D_{3d}^5$  space group and the unit cell ( $a = b = 4.135 \text{ \AA}$ ,  $c = 28.615 \text{ \AA}$ ) is highlighted in red. The structure consists of stacked quintuple layers with  $9.5 \text{ \AA}$  thickness. Atoms within a quintuple layer are covalently bonded, whereas neighboring quintuple layers are Van der Waals bonded.

gradually widen into nanoplates above  $480^\circ\text{C}$  [see Fig. 2(c)]. Longer growth runs of 30 minutes produced ribbons up to  $10 \mu\text{m}$  long, maintaining cross sections on the order of  $10 \times 100 \text{ nm}^2$ . Such  $10 \text{ nm}$  thick nanoribbons approach the  $\sim 5 \text{ nm}$  limit in which the interaction of opposite TI surface states gives rise to new effects such as thickness-based modulation of the surface gap [28, 29].

In general, nanostructure growth can occur by several mechanisms, including vapor-liquid-solid (VLS) and vapor-solid (VS) growth [30–32]. In the VLS process, a supersaturated liquid gold droplet typically nucleates crystal growth and provides control of the nanowire diameters. By contrast, VS commonly denotes crystal growth where no droplet is evident on the wire. Previous studies have shown highly anisotropic VS growth leading to nanowires in various materials and ascribe the nanowire growth to a terminal quasi-solid region of the same material as the wire, which plays the role of liquid droplet of VLS [33]. Solid-source vapor transport growth,

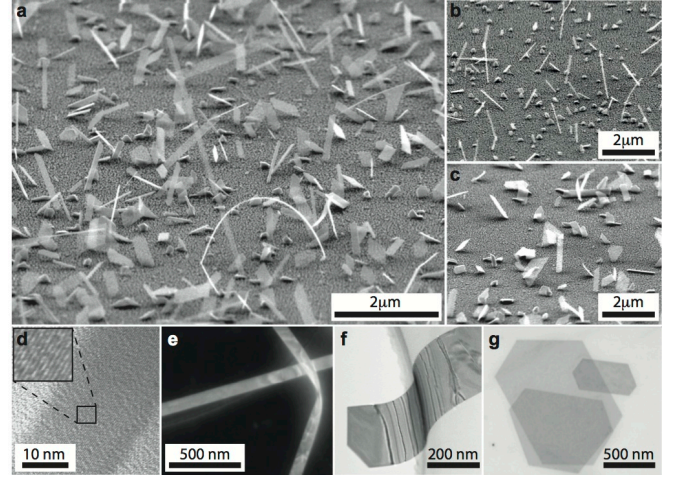


FIG. 2:  $\text{Bi}_2\text{Se}_3$  nanoribbons and platelets: (a–c) SEM images of as-grown samples, and (d–g) images obtained after the nanostructures were deposited on TEM grids. (a) Diverse growth is obtained from a  $t = 15$  minute growth run on a Si (001) substrate with  $5 \text{ nm}$  Au catalyst layer, with  $T_g = 470^\circ\text{C}$ ,  $P = 100 \text{ Torr}$ ,  $600 \text{ sccm}$   $\text{H}_2$  carrier gas flow, TMBi partial pressure  $p_{\text{TMBi}} = 1 \times 10^{-5} \text{ atm}$ , and precursor ratio  $r = 33$ . (b) A reduced precursor ratio  $r = 12$  results in narrow nanoribbons of comparatively well-defined widths  $70 \pm 20 \text{ nm}$ . (c) We obtain platelets with a precursor ratio  $r = 30$  and elevated growth temperature  $T_g = 490^\circ\text{C}$ . (d) HRTEM image of a thin ribbon,  $\sim 18 \text{ nm}$  in width. (e) Dark field scanning transmission electron microscope (STEM) image of two nanoribbons with  $85 \times 10 \text{ nm}^2$  cross section. The nanoribbons appear to be single crystal and show stress induced fringes. (f) Wide ribbon with  $230 \times 10 \text{ nm}^2$  cross section, as viewed in the TEM. (g)  $\sim 1 \mu\text{m}^2$  platelets imaged in the STEM.

in which the vapors from a heated powder of  $\text{Bi}_2\text{Se}_3$  are recrystallized onto a cooler growth substrate, has produced apparent VLS growth of  $\text{Bi}_2\text{Se}_3$  nanowires, as indicated by the presence of gold catalyst particles on the end of the wires [21]. While it has been suggested that VLS suppresses the Se vacancies in  $\text{Bi}_2\text{Se}_3$ , it is possible that growth from the Bi-rich eutectic of the Au-Bi-Se system could instead promote Se vacancies [34]. The absence of any terminal Au catalyst particle in our as-grown samples suggests VS as the growth mechanism. We believe that the Au thin film, which dramatically promotes growth, aids nucleation of the wire on the substrate, but in-situ imaging of nanowire growth may be needed to further clarify the growth mechanism [35].

We confirm the samples are high quality single crystals of  $\text{Bi}_2\text{Se}_3$  using high resolution electron microscopy. The nanostructures are first freed from the growth substrate by sonication in ethanol and then transferred to holey carbon TEM grids for imaging in a Phillips CM200 transmission electron microscope (TEM). TEM-based energy dispersive X-ray spectroscopy indicates a 2:3 ratio of Bi and Se in the nanoribbons within the 3% error of the technique, as shown in Fig. 3(b). Selected-area electron diffraction confirms the single-crystal rhombohedral

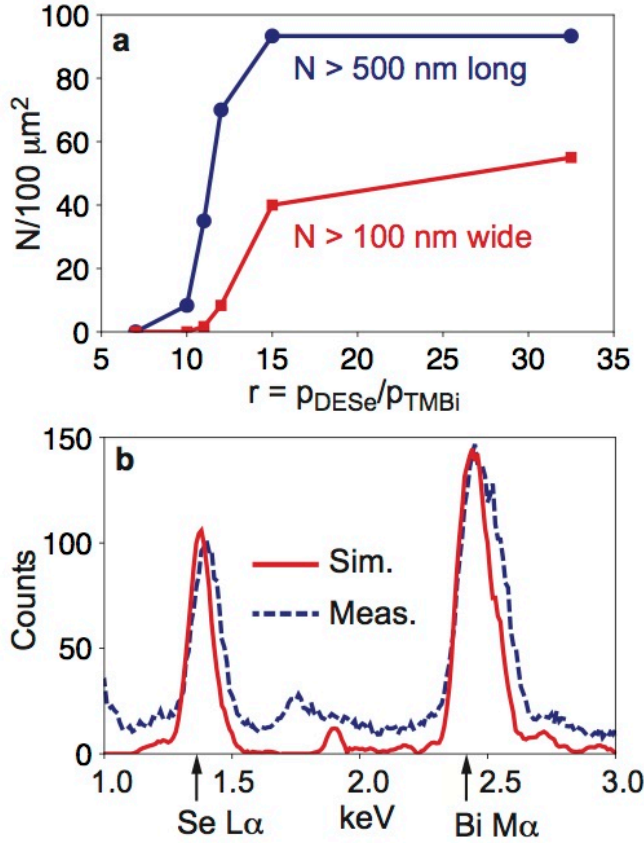


FIG. 3: (a) Growth density as a function of precursor ratio,  $r$ . At fixed growth temperature, pressure, carrier gas flow, and duration (as specified in the text) wire growth begins when  $r \geq 7$ . Further increases in the precursor ratio result in wider and longer nanoribbons. Note that at  $r = 33$ , longer wires are also present, with roughly 1/3 of the nanoribbons exceeding  $1 \mu\text{m}$  in length. (b) Energy dispersive X-ray spectrum of a thin ribbon under a 200 keV electron beam. The two peaks shown are used for measuring the Bi:Se ratio. The measured spectrum is shown by the dashed line and a Monte Carlo simulation (NIST DSTA-II) of a 10 nm film of  $\text{Bi}_2\text{Se}_3$  is shown by the solid line.

structure of ribbons, and matches the known  $\text{Bi}_2\text{Se}_3$  lattice constant spacing within experimental error ( $\pm 0.03 \text{ \AA}$ ).

Figure 4 displays high resolution TEM (HRTEM) images of the crystal lattice. The nanoribbons predominantly grow in the  $(11\bar{2}0)$  direction, normal to the  $(0001)$  QL-stacking axis, with lattice constant  $a = 4.1 \text{ \AA}$ , consistent with the spacing expected from the bulk crystal structure. The samples are exposed to atmosphere after growth and exhibit an amorphous region a few nanometers wide near the edges of the wire. The upper and lower surfaces, which lack the dangling bonds as on the edges, are expected to have significantly less irregularity. These observations, combined with recent ARPES studies of  $\text{Bi}_2\text{Se}_3$  surface reactivity, advocate the development of methods to chemically passivate the  $\text{Bi}_2\text{Se}_3$

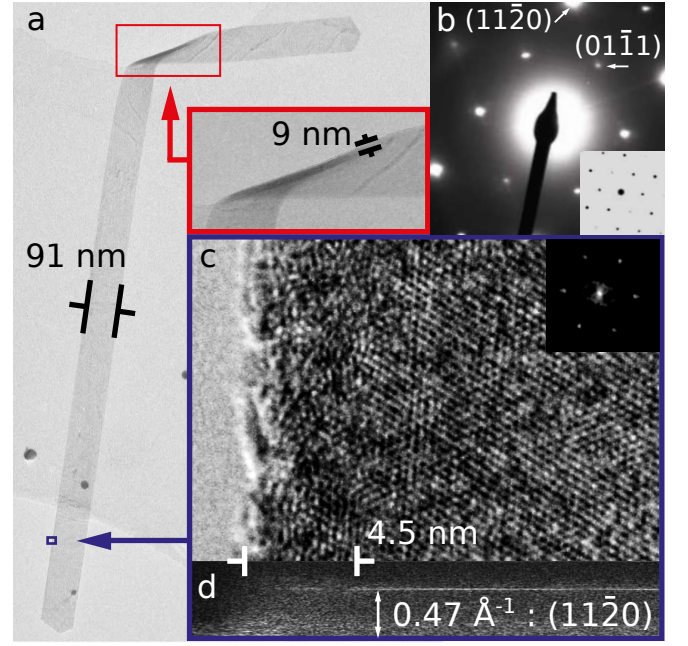


FIG. 4: (a) TEM image of a  $2 \mu\text{m}$  long, folded nanoribbon on a holey TEM grid. Growth conditions:  $T_g = 480^\circ\text{C}$ ,  $P = 100 \text{ Torr}$ ,  $t = 30 \text{ min}$ ,  $P = 600 \text{ sccm H}_2$ ,  $p_{\text{TMBi}} = 1 \times 10^{-5} \text{ atm}$ ,  $r = 30$ . A fold in the nanoribbon reveals a thickness of 9 nm. (b) TEM electron diffraction pattern. The inset shows the simulated diffraction pattern. (c) A HRTEM image shows that the nanoribbon is single crystal (inset: FFT). (d) FFT of columns of the image in (c) shows a peak at  $0.47 \text{ \AA}^{-1}$ , which is consistent with the  $(11\bar{2}0)$  growth direction. The peak fades at the edge of the nanoribbon, indicating an amorphous region with width  $\sim 4.5 \text{ nm}$ , typical of atmospherically exposed samples.

sample surface [36].

A large fraction of the nanoplates shown in Fig. 2 (a) are partially transparent in the SEM, indicating the formation of very thin nanostructures. We use TEM to quantitatively extract the sample thickness. By directly imaging the thicknesses of wires bent around the pores of the TEM grids we find an average thickness of  $\sim 10 \text{ nm}$ . An AFM study of 18 nanoribbons gives thicknesses  $20 \pm 10 \text{ nm}$ . Two examples are shown in Fig. 5 and one of the ribbons exhibits a clear 4 quintuple layer step. The nanoribbon thicknesses lie significantly below the distribution of dimensions produced by the VLS solid-source method referred to above. In particular, we find that vapor phase solid-source epitaxy typically produces ribbons 30 – 100 nm in thickness, consistent with results obtained by another group [21].

The nanostructures we obtain form a suitable basis for future TI transport experiments. They only narrowly exceed the 5–6 QL transition from 3D TI behavior to the coupled-surface regime [28]. The dependence of ribbon dimensions on growth parameters demonstrates bottom-up structural control. With proper selection of



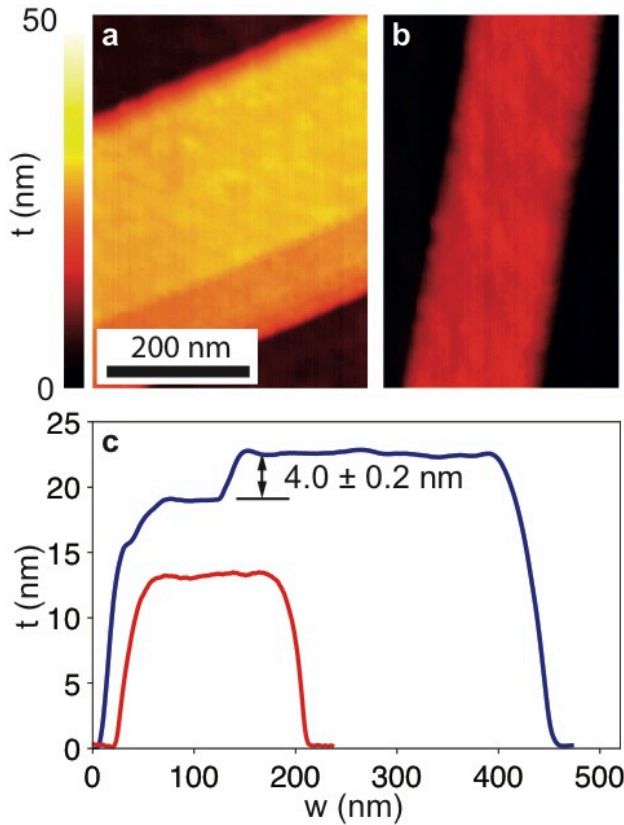


FIG. 5: AFM measurements of the nanoribbons. (a) Nanoribbon with  $\sim 23$  nm thickness. There is a 4 QL step near the lower edge of the ribbon. (b) Nanoribbon with  $\sim 13$  nm thickness. (c) Thickness profiles averaged along the length of the wires in (a–b).

substrates and growth conditions, we expect that this control will allow, for instance, arrays of aligned wires as has been achieved with other semiconductors and a tuning of the thickness through the 2D regime [37]. Perhaps more importantly, the MOCVD growth method presented here can be extended to include chemical doping or the development of ternary compounds such as  $\text{Bi}_2\text{Te}_2\text{Se}$ , for less ambiguous characterization of the surface states [12]. Aided by nanofabrication techniques, high quality nanoribbons may form the building blocks of future electronic devices based on TIs.

**Acknowledgments:** We thank Bob Cava, Sian Dutton, Minkyung Jung, Sunanda Koduvayur Parthasarathy, Chris Quintana, and Jian Zhang for technical contributions, and Nan Yao at the Princeton Imaging and Analysis Center for assistance characterizing samples. Research was supported by the Sloan and Packard Foundations, and the NSF funded Princeton Center for Complex Materials, DMR-0819860. We acknowledge the use of the PRISM Imaging and Analysis Center, which is supported in part by the NSF MRSEC program.

- [1] Hasan, M. & Kane, C. Colloquium: Topological insulators. *Rev. Mod. Phys.* **82**, 3045–67 (2010).
- [2] Qi, X.-L. & Zhang, S.-C. The quantum spin Hall effect and topological insulators. *Phys. Today* **63**, 33–8 (2010).
- [3] Xia, Y. *et al.* Observation of a large-gap topological-insulator class with a single Dirac cone on the surface. *Nature Phys.* **5**, 398–402 (2009).
- [4] Roushan, P. *et al.* Topological surface states protected from backscattering by chiral spin texture. *Nature* **460**, 1106–9 (2009).
- [5] Hor, Y. S. *et al.* p-type  $\text{Bi}_2\text{Se}_3$  for topological insulator and low-temperature thermoelectric applications. *Phys. Rev. B* **79**, 195208 (2009).
- [6] Checkelsky, J. G. *et al.* Quantum interference in macroscopic crystals of nonmetallic  $\text{Bi}_2\text{Se}_3$ . *Phys. Rev. Lett.* **103**, 246601 (2009).
- [7] Steinberg, H., Gardner, D. R., Lee, Y. S., Jarillo-Herrero, P. Surface state transport and ambipolar electric field effect in  $\text{Bi}_2\text{Se}_3$  nanodevices. *Nano Lett.* **10**, 5032–6 (2010).
- [8] Chen, J. *et al.* Gate-voltage control of chemical potential and weak antilocalization in  $\text{Bi}_2\text{Se}_3$ . *Phys. Rev. Lett.* **105**, 176602 (2010).
- [9] Das, A. *et al.* Monitoring dopants by Raman scattering in an electrochemically top-gated graphene transistor. *Nature Nanotech.* **3**, 210–5 (2008).
- [10] Peng, H. *et al.* Aharonov-Bohm interference in topological insulator nanoribbons. *Nature Mater.* **9**, 225–9 (2010).
- [11] Xiu, F. *et al.* Manipulating surface states in topological insulator nanoribbons. *Nature Nanotech.* **6**, 216–21 (2011).
- [12] Ren, Z. *et al.* Large bulk resistivity and surface quantum oscillations in the topological insulator  $\text{Bi}_2\text{Te}_2\text{Se}$ . *Phys. Rev. B* **82**, 241306 (2010).
- [13] Garate, I. & Franz, M. Inverse spin-galvanic effect in the interface between a topological insulator and a ferromagnet. *Phys. Rev. Lett.* **104**, 146802 (2010).
- [14] Fu, L. & Kane, C. Superconducting proximity effect and Majorana fermions at the surface of a topological insulator. *Phys. Rev. Lett.* **100**, 096407 (2008).
- [15] Lutchyn, R. M., Stanescu, T. D., Das Sarma, S. Search for Majorana fermions in multiband semiconducting nanowires. *Phys. Rev. Lett.* **106**, 127001 (2011).
- [16] Dresselhaus, M. S. *et al.* New directions for low-dimensional thermoelectric materials. *Adv. Mater.* **19**, 1043–53 (2007).
- [17] Pérez Vicente, C. *et al.* X-ray diffraction and  $^{119}\text{Sn}$  Mössbauer spectroscopy study of a new phase in the  $\text{Bi}_2\text{Se}_3$ - $\text{SnSe}$  system:  $\text{SnBi}_4\text{Se}_7$ . *Inorg. Chem.* **38**, 2131–5 (1999).
- [18] Hong, S. S. *et al.* Ultrathin topological insulator  $\text{Bi}_2\text{Se}_3$  nanoribbons exfoliated by atomic force microscopy. *Nano Lett.* 3118–22 (2010).
- [19] Cui, H. *et al.* Synthesis of  $\text{Bi}_2\text{Se}_3$  thermoelectric nanosheets and nanotubes through hydrothermal co-reduction method. *J. Solid State Chem.* **177**, 4001–6 (2004).
- [20] Jagminas, A., Valsiunas, I., Veronese, G., Juskenas, R. & Rutavicius, A. Alumina template-assisted growth of bismuth selenide nanowire arrays. *J. Cryst. Growth* **310**, 428–33 (2008).

- [21] Kong, D. *et al.* Topological insulator nanowires and nanoribbons. *Nano Lett.* **10**, 329–33 (2010).
- [22] Al Bayaz, A. Growth parameters effect on the electric and thermoelectric characteristics of  $\text{Bi}_2\text{Se}_3$  thin films grown by MOCVD system. *J. Cryst. Growth* **241**, 463–70 (2002).
- [23] Seshan, K. (ed.) *Handbook of Thin-Film Deposition Processes and Techniques* (William Andrew Publishing/Noyes, Norwich, NY, 2002), 2nd edn.
- [24] Lin, Y.-F., Chang, H.-W., Lu, S.-Y., Liu, C.W. Preparation, characterization, and electrophysical properties of nanostructured  $\text{BiPO}_4$  and  $\text{Bi}_2\text{Se}_3$  derived from a structurally characterized, single-source precursor  $\text{Bi}[\text{Se}_2\text{P}(\text{OiPr})_2]_3$ . *J. Phys. Chem. C* **111**, 18,538–18,544 (2007).
- [25] Schroer, M. D., Xu, S. Y., Bergman, A. M. & Petta, J. R. Development and operation of research-scale III-V nanowire growth reactors. *Rev. Sci. Instrum.* **81**, 023903 (2010).
- [26] Schroer, M. D., Petta, J. R. Correlating the nanostructure and electronic properties of InAs nanowires. *Nano Lett.* **10**, 1618–22 (2010).
- [27] Precursors are available from Strem Chemicals Inc. and SAFC Hitech.
- [28] He, K. *et al.* Crossover of the three-dimensional topological insulator  $\text{Bi}_2\text{Se}_3$  to the two-dimensional limit. *Nature Phys.* **6**, 584–8 (2010).
- [29] Lu, H.-Z., Shan, W.-Y., Yao, W., Niu, Q. & Shen, S.-Q. Massive Dirac fermions and spin physics in an ultrathin film of topological insulator. *Phys. Rev. B* **81**, 115407 (2010).
- [30] Duan, X.F., Lieber, C.M. General synthesis of compound semiconductor nanowires. *Adv. Mater.* **12**, 398–402 (2000).
- [31] Kolasinski, K. Catalytic growth of nanowires: vapor–liquid–solid, vapor–solid–solid, solution–liquid–solid and solid–liquid–solid growth. *Curr. Opin. Solid St. M.* **10**, 182–91 (2006).
- [32] Mohammad, S. N. General hypothesis governing the growth of single-crystal nanowires. *J. Appl. Phys.* **107**, 114304 (2010).
- [33] Hsu, Y.-J. & Lu, S.-Y. Vapor-solid growth of Sn nanowires: growth mechanism and superconductivity. *J. Phys. Chem. B* **109**, 4398–403 (2005).
- [34] Prince, A., Raynor, G. V. & Evans, D. S. *Phase Diagrams of Ternary Gold Alloys* (Institute of Metals, London, 1990).
- [35] Ross, F. M. Controlling nanowire structures through real time growth studies. *Rep. Prog. Phys.* **73**, 114501 (2010).
- [36] Chen, Y. L. *et al.* Massive Dirac fermion on the surface of a magnetically doped topological insulator. *Science* **329**, 659–62 (2010).
- [37] Tomioka, K. *et al.* Growth of highly uniform InAs nanowire arrays by selective-area MOVPE. *J. Cryst. Growth* **298**, 644–7 (2007).